



UNIVERSITY OF LEEDS

This is a repository copy of *Cation doping and oxygen vacancies in the orthorhombic FeNbO₄ material for solid oxide fuel cell applications: A density functional theory study*.

White Rose Research Online URL for this paper:

<https://eprints.whiterose.ac.uk/212438/>

Version: Accepted Version

Article:

Wang, X., Santos-Carballal, D. orcid.org/0000-0002-3199-9588 and de Leeuw, N.H. orcid.org/0000-0002-8271-0545 (2024) Cation doping and oxygen vacancies in the orthorhombic FeNbO₄ material for solid oxide fuel cell applications: A density functional theory study. *The Journal of Chemical Physics*, 160 (15). 154713. ISSN 0021-9606

<https://doi.org/10.1063/5.0192749>

© 2024 Author(s). Published under an exclusive license by AIP Publishing. This article may be downloaded for personal use only. Any other use requires prior permission of the author and AIP Publishing. The following article appeared in Wang, X., Santos-Carballal, D. and de Leeuw, N.H. (2024) Cation doping and oxygen vacancies in the orthorhombic FeNbO₄ material for solid oxide fuel cell applications: A density functional theory study. *The Journal of Chemical Physics*, 160 (15). 154713. ISSN 0021-9606 and may be found at <https://doi.org/10.1063/5.0192749>. Uploaded in accordance with the publisher's self-archiving policy.

Reuse

Items deposited in White Rose Research Online are protected by copyright, with all rights reserved unless indicated otherwise. They may be downloaded and/or printed for private study, or other acts as permitted by national copyright laws. The publisher or other rights holders may allow further reproduction and re-use of the full text version. This is indicated by the licence information on the White Rose Research Online record for the item.

Takedown

If you consider content in White Rose Research Online to be in breach of UK law, please notify us by emailing eprints@whiterose.ac.uk including the URL of the record and the reason for the withdrawal request.



eprints@whiterose.ac.uk
<https://eprints.whiterose.ac.uk/>

Cation Doping and Oxygen Vacancies in the Orthorhombic FeNbO₄ Material for Solid Oxide Fuel Cell Applications: A Density Functional Theory Study

Xingyu Wang¹, David Santos-Carballal^{1*}, Nora H. de Leeuw^{*1,2}

¹ School of Chemistry, University of Leeds, Leeds LS2 9JT, United Kingdom

² Department of Earth Sciences, Utrecht University, 3584 CB Utrecht, The Netherlands

d.santos-carballal@leeds.ac.uk; n.h.deleeuw@leeds.ac.uk

Abstract

The orthorhombic phase of FeNbO₄, a promising anode material for solid oxide fuel cells (SOFC), exhibits good catalytic activity towards hydrogen oxidation. However, the low electronic conductivity of the material specifically in the pure structure without defects or dopants limits its practical applications as an SOFC anode. In this study, we have employed density functional theory (DFT + *U*) calculations to explore the bulk and electronic properties of two types of doped structures, Fe_{0.9375}A_{0.0625}NbO₄ and FeNb_{0.9375}B_{0.0625}O₄ (*A, B* = Ti, V, Cr, Mn, Co, Ni) and the oxygen-deficient structures Fe_{0.9375}A_{0.0625}Nb₁O_{3.9375} and FeNb_{0.9375}B_{0.0625}O_{3.9375}, where the dopant is positioned in the first nearest neighbour (1st NN) site to the oxygen vacancy. Our DFT simulations have revealed that doping in the Fe sites is energetically favourable compared to doping in the Nb site, resulting in significant volume expansion. The doping process generally requires less energy when the O-vacancy is surrounded by one Fe and two Nb ions. The simulated projected density of states (PDOS) of the oxygen-deficient structures indicates that doping in the Fe site, particularly with Ti and V, considerably narrows the band gap to ~0.5 eV, whereas doping with Co at the Nb sites generates acceptor levels close to 0 eV. Both doping schemes therefore enhance electron conduction during SOFC operation.

27 **1. Introduction**

28 FeNbO₄ gained initial recognition as a hydrogen sensor in the early 21th century¹⁻⁹. In recent
29 years, research on this material has diversified into various applications, including as dielectric
30 ceramic materials¹⁰⁻¹³, anode materials for lithium-ion batteries and catalytic electrodes¹⁴⁻²³.
31 Notably, exploration of the orthorhombic phase with a disordered cation distribution as an
32 alternative material for solid oxide fuel cell (SOFC) anodes has provided new insights into the
33 stability and catalytic performance of such Fe-based anode materials^{17, 19}. Previous
34 experimental studies have shown that the orthorhombic FeNbO₄ anode material exhibits robust
35 resistance to sulphur poisoning and a good electric conductivity of $\sim 0.7 \text{ S}\cdot\text{cm}^{-1}$, which is over
36 ten times larger than the commonly used La_{0.75}Sr_{0.25}Cr_{0.5}Mn_{0.5}O₃²⁴⁻²⁶ anode.

37 Despite these promising attributes, our previous work and other experimental results³⁰⁻³³, have
38 revealed that the band gap of the pure orthorhombic FeNbO₄ material is around 2.2 eV, which
39 limits its electronic conductivity. To address this limitation, Ti⁴⁺ dopants have been introduced
40 to substitute both Fe³⁺ and Nb⁵⁺ ions¹⁹. However, the full impact of these dopants on the
41 structural and electronic properties remains poorly understood. In this study, we have
42 substitutionally doped the Fe and Nb sites of both the stoichiometric and O-deficient
43 orthorhombic FeNbO₄ structure by the first-row transition metal atoms Ti, V, Cr, Mn, Co and
44 Ni. We have employed calculations based on the density functional theory (DFT) to evaluate
45 the feasibility of incorporating these dopants into the material, fully characterising their effect
46 on the structural and electronic properties, which is crucial in guiding future experimental work.

47 **2. Computational Methods**

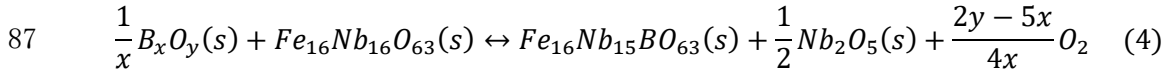
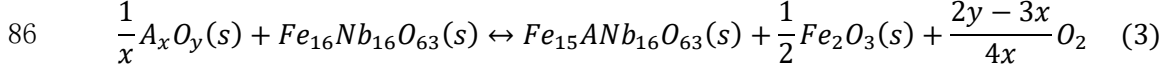
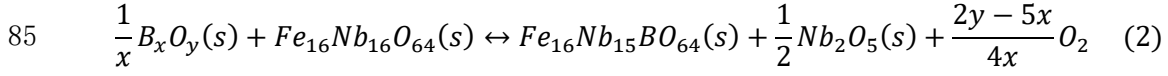
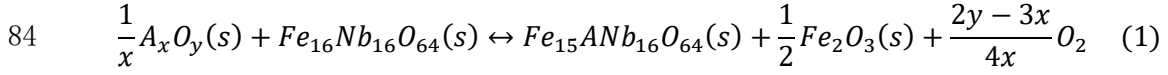
48 **2.1. DFT calculations**

49 We have employed the Vienna Ab initio Simulation Package, VASP (version 5.4.4)³⁴⁻³⁷, to
50 carry out the DFT calculations of the FeNbO₄ models. The frozen ion-electron interactions were
51 modelled using the projector-augmented wave method (PAW)³⁸. We have treated the following
52 as valence electrons: Fe(3p⁶3d⁷4s¹), Nb(4p⁶5s¹4d⁴4s²), O(2s²2p⁶), Ti(3s²3p⁶3d²4s²),
53 V(3s²3p⁶3d⁴4s¹), Cr(3p⁶3d⁵4s¹), Mn(3p⁶3d⁵4s²), Co(3p⁶3d⁷4s²) and Ni (3p⁶3d⁸4s²). Despite
54 partially breaking the Aufbau principle and differing from the ground state valence electronic

55 configuration of the free atoms, VASP contains pseudopotential files using $3d^74s^1$ for Fe and
56 $3d^44s^1$ for V, which resemble more closely the ground state valence electron distribution
57 simulated in the bulk phases of these metals.^{39,40} The valence electrons are allowed to relax
58 during our simulations and therefore the references used for the valence electron distribution of
59 these atoms are not really important, as they are identical across all our calculations. We have
60 used the Perdew-Burke-Ernzerhof (PBE) generalized gradient approximation (GGA)⁴¹
61 exchange-correlation functional for all the spin-polarized calculations. Partial occupancies were
62 taken into account using the tetrahedron method with Blöchl corrections. The magnetic
63 structure considered in this work is illustrated in Figure 1 and the rationale for this choice is
64 discussed in section 3.1. To enhance the description of the electronic structures, we have
65 incorporated the on-site Coulombic interaction (DFT+U)⁴² for Fe-3d, Ti-3d, V-3d, Cr-3d, Mn-
66 3d, Co-3d and Ni-3d electrons with the U_{eff} values set at 4.3 eV, 3.5 eV, 3.5 eV, 3.5 eV, 4.0 eV,
67 4.5 eV and 5.0 eV, respectively, based on previous studies²⁶. After test calculations, the kinetic
68 energy cut-off for the plane wave basis set was set at 500 eV, and the Henkelman algorithm
69 was employed to calculate the Bader charges⁴³. A $3\times 3\times 3$ gamma-centered Monkhorst-Pack
70 grid was used to simulate the bulk models and structural optimisations were carried out using
71 the conjugate gradient method, terminating when forces were converged within $0.01 \text{ eV}/\text{\AA}$. The
72 electronic energy was considered optimised when it exhibited a change of less than 10^{-5} eV
73 between two consecutive self-consistent loops.

74 **2.2. Doping energy**

75 We represent the doping process in both stoichiometric ($Fe_{16}Nb_{16}O_{64}$) and O-deficient
76 $Fe_{16}Nb_{16}O_{63}$ using the Kröger-Vink notation equations 1-4. This notation is a set of
77 conventions employed to describe the positions of point defects and charges within the crystal.
78 We have designated A/B_xO_y as the metal oxide phases TiO_2 , V_2O_5 , Cr_2O_3 , MnO_2 , Co_3O_4 and
79 NiO in their most stable structures, *i.e.* with the space groups $P4_2/mnm$, $P2_1/m$, $R\bar{3}c$, $P4_2/mnm$,
80 $Fd\bar{3}m$ and $Fm\bar{3}m$, respectively. The lattice parameters for these structures are listed in Table
81 S1. Note that the coefficient of O_2 is negative when the structure is doped with NiO at the Fe
82 site and NiO, Cr_2O_3 , MnO_2 and Co_3O_4 at the Nb site, indicating that this gas molecule is a
83 reactant and not a product.



88 The doping energy (E_{doping}) is calculated as the sum of the energies of the products minus the
 89 sum of the energies of the reactants multiplied by their respective coefficients in the chemical
 90 equations 1 to 4.

91 **3. Results and Discussion**

92 First, we have investigated the impact of the transition metal dopants on the structural and
 93 electronic properties of FeNbO₄. We have employed both the ordered stoichiometric structure
 94 and the O-deficient structure in the configuration with the largest probability, as identified in
 95 our previous work, see Figure 1.³⁰ It is crucial to note that the lowest energy stoichiometric
 96 FeNbO₄ structure exhibits an ordered distribution of cations, characterised by a single ionic
 97 arrangement, whereas the O-deficient structure is disordered and is represented by multiple
 98 configurations³⁰. In this work, we have used the 2×2×2 supercell of FeNbO₄, which size is
 99 sufficient to capture the random cation distribution and simulate the bulk properties of the
 100 doped $Fe_{0.9375}A_{0.0625}NbO_4/FeNb_{0.9375}B_{0.0625}O_4$ and oxygen-deficient
 101 $Fe_{0.9375}A_{0.0625}NbO_{3.9375}/FeNb_{0.9375}B_{0.0625}O_{3.9375}$ configurations. Specifically, when introducing
 102 one dopant atom into the Fe or Nb sites of the 2×2×2 supercell, the stoichiometry was reduced
 103 from 1 to 0.9375, where the subscript 3.9375 means that one oxygen vacancy was generated in
 104 the simulation cell. After testing various magnetic structures, we determined that the
 105 stoichiometric material adopts an antiferromagnetic configuration, where the alternating Fe
 106 layers along the c axis have opposite spin directions, see Figures 1 (a) and S1. In contrast, the
 107 most stable configuration for the O-deficient structure involves spins of the Fe in the layer
 108 containing only these cations aligning in the opposite direction to the spins in the mixed layers,
 109 which are parallel, as shown in Figure 1 (b).

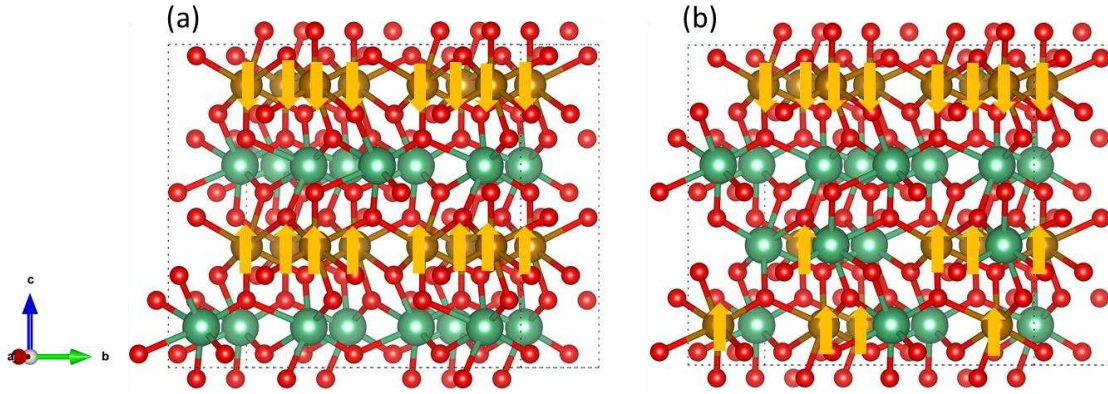


Figure 1 (a) Stoichiometric and (b) O-deficient structures showing the magnetic configurations employed in this study. O is shown in red, Fe in brown and Nb in green.

3.1 Effect of dopants on FeNbO₄

3.1.1 Structural properties

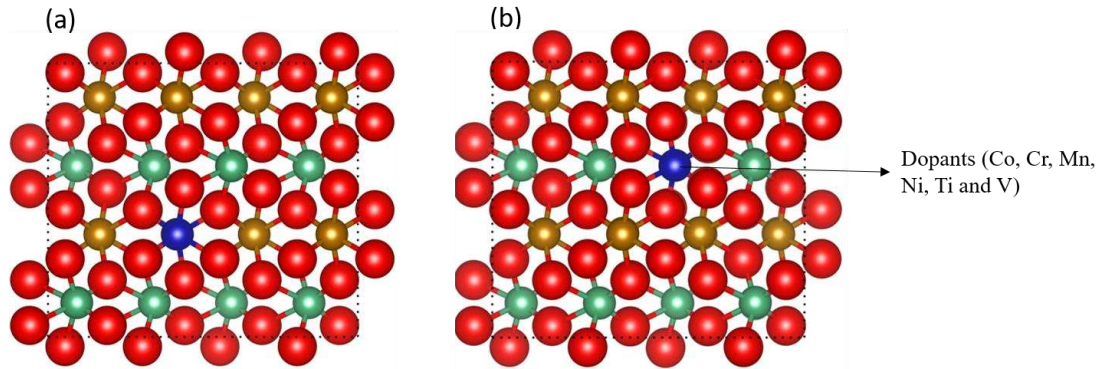
The stoichiometric FeNbO₄, modelled as a 2×2×2 supercell and belonging to the space group Pbcn, comprises 16 Fe, 16 Nb and 64 O atoms (Fe₁₆Nb₁₆O₆₄). Given that all Fe and Nb ions reside in the same Wyckoff 4c site, our approach involves selectively substituting one Fe and one Nb site at a time for the doping process, see Figure 2. Initially, we have scrutinised the effect of dopants in the Fe site on the lattice parameters, which are summarised in Table 1. Across all structures with dopants in the Fe site, we observed a tendency for lattice elongation along the *a* axis, while the Co and Ni dopants resulted in a reduction of the *b* and *c* lengths of the cell. Our computations indicate that post-doping, the α and γ angles of all structures have remained at 90°, while the β angle deviated by no more than 0.08° from the ideal right angle of the parent material. The *y* coordinate experienced a slight overestimation in comparison to the ideal 4c Wyckoff position value of 0.1786. Additionally, we have computed the volume as $V =$

$a \times b \times c \times \sqrt{1 - \cos^2\alpha - \cos^2\beta - \cos^2\gamma + 2\cos\alpha\cos\beta\cos\gamma}$ and the volume change as

$\frac{\Delta V}{V} = \frac{V_{doped} - V_{undoped}}{V_{undoped}}$. Our findings indicate that structures doped with Co or Ni underwent a

marginal compression along the *b* and *c* directions. In contrast, doping with Ti, V, Cr and Mn led to a volume expansion with the Ti-doped structure exhibiting the most significant increase at 0.368%. Notably, the observed effects of first row transition metal dopants on volume align closely with previous research, where the introduction of Ti and Cr on the Mn site of NaMnO₂

133 resulted in volume stretching, while Co and Ni, possessing larger atomic numbers than Mn, led
 134 to volume compression⁴⁴.



135

136 **Figure 2 Optimised structures of FeNbO₄ with Co, Cr, Mn, Ni, Ti and V dopants on the (a) Fe**
 137 **site and (b) Nb site; O is red, Fe is brown, Nb is green and dopants are dark blue.**

138 **Table 1. Lattice parameters, y coordinate of dopants and volume of the FeNbO₄ structure with**
 139 **dopants incorporated at the Fe site.**

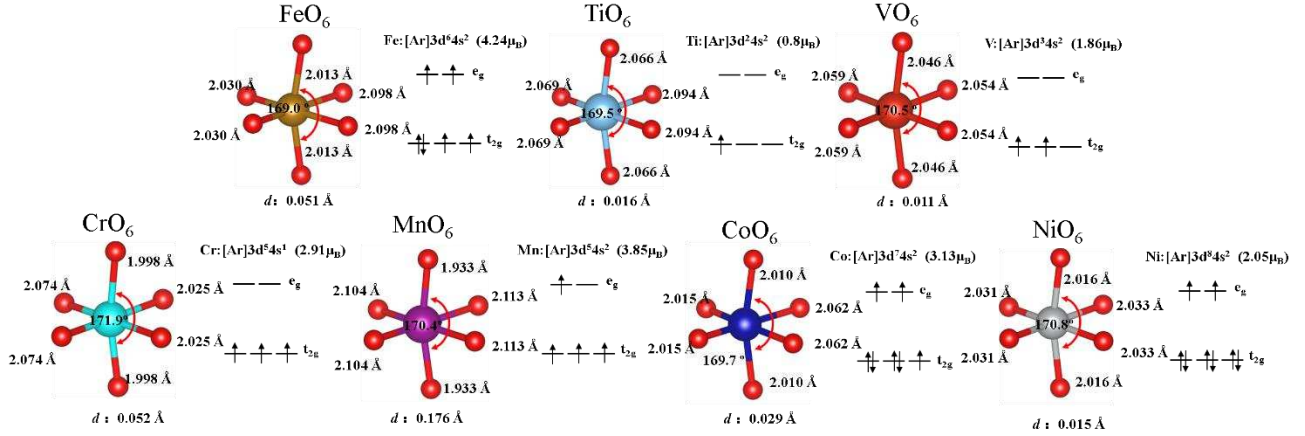
<i>A, B</i>	<i>a</i> (Å)	<i>b</i> (Å)	<i>c</i> (Å)	α (°)	β (°)	γ (°)	<i>y</i>	<i>V</i> (Å ³)	$\Delta V/V$ (%)
Stoichiometric	9.407	11.380	10.046	90	90	90	0.1786	1075.627	-
Ti	9.421	11.388	10.062	90	90.01	90	0.1809	1079.584	0.368
V	9.414	11.387	10.056	90	89.94	90	0.1828	1077.887	0.210
Cr	9.411	11.382	10.048	90	89.97	90	0.1858	1076.271	0.060
Mn	9.417	11.394	10.039	90	90.15	90	0.1823	1077.232	0.149
Co	9.412	11.376	10.045	90	89.97	90	0.1806	1075.459	-0.015
Ni	9.408	11.375	10.045	90	89.92	90	0.1833	1075.045	-0.054

140

141 For a transition metal atom with an octahedral geometry, the five d orbitals are split into three
 142 degenerate lower-energy t_{2g} orbitals and two degenerate higher-energy e_g orbitals. However,
 143 those orbitals are unstable and break the degeneracy resulting in the elongation or shortening
 144 of one of the three C_4 rotation axes, which is known as the Jahn-Teller distortion. We found
 145 that the octahedral geometries of all dopants, also including Fe and Nb in the stoichiometric
 146 structure, show Jahn-Teller distortion where each of the three pairs of identical bonds have
 147 different lengths to the other two and the axial angle deviates from 180° , see Figures 3 and 4.
 148 We have calculated the Jahn-Teller distortion as $d_{JT} = (d_{e1} + d_{e2})/2 - d_a$, where d_{e1} , d_{e2} and

149 d_a indicate the equatorial bond distances 1 and 2 and the axial bond distance, respectively. Our
150 simulations show that the uneven occupation of electrons in e_g orbitals leads to a stronger Jahn-
151 Teller distortion than the partial occupation of the t_{2g} orbitals, as found in previous reports^{45,46}.
152 For example, the single electron in the e_g orbital of Mn leads to the largest distortion of 0.176
153 Å found in this work when doping into the Fe sites of the stoichiometric structure. In addition,
154 we found weak Jahn-Teller distortions of Fe, Ti, V and Co octahedra below 0.051 Å because
155 of the uneven occupation of electrons in the t_{2g} levels. For the Cr and Ni dopants, the electrons
156 are distributed evenly in the t_{2g} or e_g levels and thus, we would not expect distortion. However,
157 we found weak distortions of 0.052 Å and 0.015 Å for Cr and Ni, respectively, that are even
158 larger than for other ions with uneven occupation of the t_{2g} orbitals. The Jahn-Teller distortion
159 found here follows the order $d_{JT}(\text{Mn}) > d_{JT}(\text{Fe}) > d_{JT}(\text{Cr}) > d_{JT}(\text{Co}) > d_{JT}(\text{Ti}) >$
160 $d_{JT}(\text{Ni}) > d_{JT}(\text{V})$.

161 Our calculations indicate that the t_{2g} and e_g levels of Nb are empty in the stoichiometric
162 structure. We also found that after doping the Nb site with Ti and V, the t_{2g} and e_g remain
163 unoccupied, whereas only three electrons occupy the t_{2g} level of the Mn dopant, which explains
164 the weak Jahn-Teller distortions of up to $d_{JM} = 0.092$ Å for the V ion, see Figure 4. Despite an
165 odd number of electrons distributed in the e_g level of Ni, we only found a small Jahn-Teller
166 effect with a distortion of 0.053 Å. Cr and Co with a high spin electron distribution should
167 exhibit weak Jahn-Teller distortions owing to the uneven occupation of their t_{2g} orbitals.
168 However, we found large distortions of 0.176 and 0.132 Å for Cr and Co, respectively. Note
169 that the distortion of the axial angle is larger for the dopants in the Nb site than in the Fe site.
170 We speculate that the lack of correlation between the expected weak and strong Jahn-Teller
171 distortions can be explained not only by the elongation or shortening of the axial bond, but also
172 by the bending of the axial axis. We do not discuss the Jahn-Teller effect in the O-deficient
173 structures because the introduction of oxygen vacancies leads to dangling bonds.



174

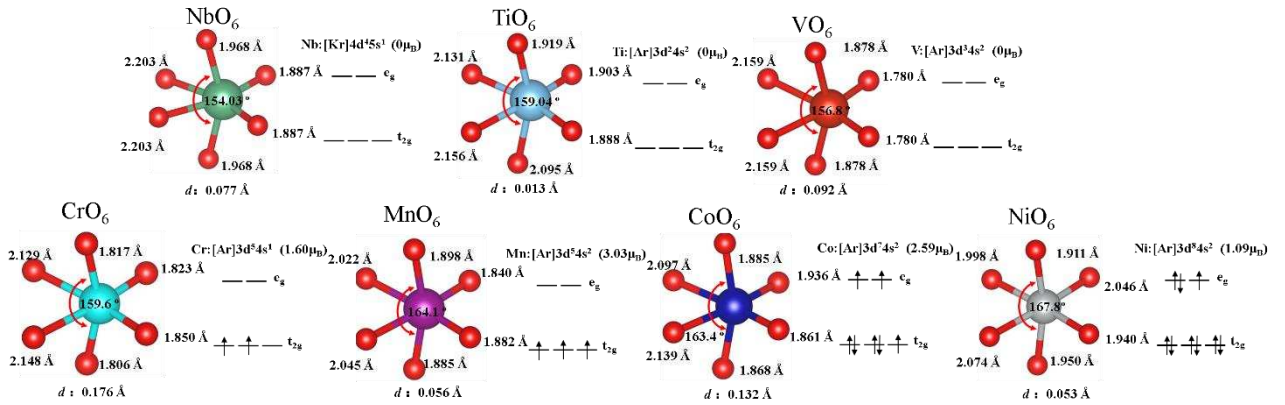
175

176

177

178

Figure 3. Octahedral geometry and orbital splitting of dopants in the Fe site of the stoichiometric structure. The Jahn-Teller distortion is defined as $d_{JT} = (d_{e1} + d_{e2})/2 - d_a$, where d_{e1} , d_{e2} and d_a indicate the equatorial bond distances 1 and 2 and the axial bond distance, respectively.



179

180

181

182

183

184

185

186

187

188

189

190

Figure 4. Octahedral geometry and orbital splitting of dopants in the Nb site of the stoichiometric structure. The Jahn-Teller distortion is defined as $d_{JT} = (d_{e1} + d_{e2})/2 - d_a$, where d_{e1} , d_{e2} and d_a indicate the equatorial bond distances 1 and 2 and the axial bond distance, respectively.

Table 2 shows that structures containing dopants at the Nb sites are compressed in all three crystallographic directions, barring the expanded c parameter observed in the Ti-doped structure. Our simulations show that the lattice structure tends to adopt a triclinic form, with all lattice angles deviating from 90° by no more than 0.18° . Furthermore, the y coordinates of dopants at the Nb sites tend to be underestimated compared to the value in the parent material of 0.1786, except for the structure containing V. Our calculated volumes for the doped structures are consistently smaller than those of pure FeNbO₄, with the Mn-doped material,

191 exhibiting the most significant reduction of 0.556%. In general, our findings indicate that
 192 doping the Nb site induces a greater degree of symmetry breaking compared to doping the Fe
 193 site, resulting in the formation of triclinic structures. Crucially, our calculations reveal a volume
 194 decrease solely for $\text{FeNb}_{0.9375}\text{B}_{0.0625}\text{O}_4$, with respect to FeNbO_4 , underscoring the prominent role
 195 of Nb site doping in reducing the overall volume of the material.

196 **Table 2. Lattice parameters, y coordinate of dopants and volume of the FeNbO_4 structure with**
 197 **dopants incorporated at the Nb site.**

<i>A, B</i>	<i>a</i> (Å)	<i>b</i> (Å)	<i>c</i> (Å)	α (°)	β (°)	γ (°)	<i>y</i>	<i>V</i> (Å ³)	$\Delta V/V$ (%)
Stoichiometric	9.407	11.380	10.046	90	90	90	0.1786	1075.627	-
Ti	9.402	11.374	10.052	89.97	89.82	90.06	0.1764	1075.036	-0.055
V	9.390	11.378	10.031	90	89.92	90	0.1817	1071.851	-0.351
Cr	9.387	11.380	10.026	89.97	89.90	90.05	0.1750	1071.000	-0.430
Mn	9.383	11.355	10.039	90.04	89.82	90.02	0.1630	1069.650	-0.556
Co	9.391	11.369	10.034	89.91	89.95	89.93	0.1684	1071.420	-0.391
Ni	9.385	11.368	10.038	89.85	89.83	90.16	0.1525	1071.011	-0.429

198

199 The Bader charges for both $\text{Fe}_{0.9375}\text{A}_{0.0625}\text{NbO}_4$ and $\text{FeNb}_{0.9375}\text{B}_{0.0625}\text{O}_4$ structures are presented
 200 in Table 3. We observe a consistent decrease in the Bader charges of first row transition metal
 201 dopants at the Fe site, following the order $q_{\text{Ti}} > q_{\text{V}} > q_{\text{Cr}} \approx q_{\text{Mn}} > q_{\text{Co}} > q_{\text{Ni}}$, which is consistent
 202 with their respective positions in the periodic table. Our calculations indicate that the Bader
 203 charges of O, Fe, and Nb remain constant with respect to the stoichiometric structure, except
 204 for Ti- and V-doped structures, where the Bader charge of oxygen exhibits a marginal increase.
 205 We noted a similar trend in the Bader charges of dopants between $\text{FeNb}_{0.9375}\text{B}_{0.0625}\text{O}_4$ and
 206 $\text{Fe}_{0.9375}\text{A}_{0.0625}\text{NbO}_4$. Our DFT calculations indicate that Bader charges of dopants tend to be
 207 larger at the Nb site than at the Fe site. This observation suggests a greater likelihood for the
 208 Nb site to form stronger ionic interactions with the crystal than its Fe counterpart.

209 **Table 3 Atomic Bader charges (*q*) in the doped FeNbO_4 structure.**

<i>A, B</i>	Fe site				Nb site			
	$q_{\text{A}}(\text{e})$	$q_{\text{O}}(\text{e})$	$q_{\text{Fe}}(\text{e})$	$q_{\text{Nb}}(\text{e})$	$q_{\text{B}}(\text{e})$	$q_{\text{O}}(\text{e})$	$q_{\text{Fe}}(\text{e})$	$q_{\text{Nb}}(\text{e})$

Stoichiometric	-	-1.14	+1.86	+2.72	-	-1.14	+1.86	+2.72
Ti	+2.11	-1.15	+1.86	+2.72	+2.44	-1.14	+1.86	+2.72
V	+1.97	-1.15	+1.86	+2.72	+2.31	-1.14	+1.86	+2.72
Cr	+1.84	-1.14	+1.86	+2.72	+2.06	-1.13	+1.86	+2.72
Mn	+1.81	-1.14	+1.86	+2.72	+1.92	-1.13	+1.86	+2.72
Co	+1.67	-1.14	+1.86	+2.72	+1.63	-1.13	+1.86	+2.72
Ni	+1.52	-1.14	+1.86	+2.72	+1.41	-1.12	+1.86	+2.72

210

211 Next, we have calculated the magnetic moments of the cations in the stoichiometric and doped
212 materials, shown in Table 4. The magnetic moment of Fe is underestimated at 4.27 μ_B , a value
213 in close agreement with previous findings³³. The magnetic moments of the dopants tend to
214 increase with atomic number from Ti to Mn, followed by a decrease from Mn to Ni. Moreover,
215 the valence states of cations in the stoichiometric and doped materials can be deduced from
216 their magnetic moments. In the $\text{Fe}_{0.9375}\text{A}_{0.0625}\text{NbO}_4$ structure, we have approximated the
217 magnetic moments of dopants to the nearest integer, resulting in $m_s(\text{Fe}) = 5 \mu_B$, $m_s(\text{Nb}) = 0 \mu_B$,
218 $m_s(\text{Ti}) = 1 \mu_B$, $m_s(\text{V}) = 2 \mu_B$, $m_s(\text{Cr}) = 3 \mu_B$, $m_s(\text{Mn}) = 4 \mu_B$, $m_s(\text{Co}) = 3 \mu_B$, and $m_s(\text{Ni}) = 2 \mu_B$.
219 All cations, including dopants, are in octahedral coordination, splitting the 3d orbital into three
220 degenerate t_{2g} orbitals (d_{xy} , d_{xz} and d_{yz}) and two also degenerate e_g orbitals ($d_{x^2-y^2}$, and d_{z^2}).
221 Specific magnetic arrangements for Fe-substituted structures reveal that Cr, Mn, Ti and V are
222 in the +3 valence state, while Co and Ni are in the +2 oxidation state. Additionally, we have
223 calculated the magnetic moment of dopants at the Nb site, all displaying a relatively low-spin
224 state. Our calculations show that only the valence state of Ni was underestimated at +1, which
225 is a state uncommon for Ni. Comparing valence states in both the Fe and Nb sites, we observe
226 that, except for the Co dopant, the magnetic moments of the other dopants are lower than the
227 corresponding values at the Fe site. This correlates with an increase in valence states from +2
228 to +4 for Cr, Mn and Ti and from +3 to +5 for V. Furthermore, the valence states of Co and Ni
229 in the $\text{Fe}_{0.9375}\text{A}_{0.0625}\text{NbO}_4$ structure is smaller than that of the substituted Fe^{3+} , suggesting that
230 oxygen donated electrons to these two dopants, a trend which is also evident in Ti-, Cr-, Mn-,
231 Co- and Ni-doped $\text{FeNb}_{0.9375}\text{B}_{0.0625}\text{O}_4$ structures.

232 **Table 4. Atomic magnetic moments (m_s), and valence states (VS) of the doped FeNbO₄ structure.**

<i>A, B</i>	Fe site		Nb site	
	m_s (μ_B)	VS	m_s (μ_B)	VS
Stoichiometric	4.27-(Fe)	+3	0-(Nb)	+5
Ti	0.80	+3	0	+4
V	1.86	+3	0	+5
Cr	2.91	+3	1.60	+4
Mn	3.85	+3	3.03	+4
Co	3.13	+2	2.59	+2
Ni	2.05	+2	1.09	+1

233

234

235 The Shannon's effective radius for each dopant and their doping energies into FeNbO₄ are
 236 detailed in Table 5. Shannon's reported effective ionic radii²⁶ are contingent on the valence and
 237 spin states of the transition metal atom. When Co and Mn occupy the Fe site, two possible
 238 magnetic structures emerge: high-spin states with magnetic moments of 3 and 4 μ_B , respectively,
 239 or low-spin states, with magnetic moments of 1 and 2 μ_B , respectively, see Figure 4. Our
 240 calculations indicate that the magnetic moments of Co and Mn align closely with high-spin
 241 states, measuring 3 and 4 μ_B , respectively. In contrast, Ti, V, Cr and Ni exhibit only one
 242 magnetic configuration, as illustrated in Figure 4. Our calculations show that only Ti³⁺
 243 possesses a larger radius (0.670 Å) than Fe³⁺ in the parent structure, whereas Mn³⁺ and Fe³⁺
 244 have very similar sizes, which is expected from their relative positions in the periodic table, see
 245 Table 5. Furthermore, the radii of V³⁺ and Cr³⁺ atoms, calculated as 0.640 and 0.615 Å,
 246 respectively, are smaller than Fe³⁺. In contrast, Co²⁺ and Ni²⁺ feature larger radii than Fe³⁺,
 247 attributed to their distinct oxidation states. The calculated doping energies imply that inserting
 248 V³⁺, Cr³⁺ or Mn³⁺ is generally more facile than replacing Fe with Co²⁺, Ni²⁺ or Ti³⁺.
 249 Additionally, we found that dopant size correlates with doping energy, evidenced by the
 250 sequence $R_{Co} > R_{Ni} > R_{Ti} > R_{Mn} > R_V > R_{Cr}$ and the order of doping energy as $E_{Ti} > E_{Co} > E_{Ni} >$
 251 $E_V > E_{Mn} > E_{Cr}$. This suggests that dopants with smaller radii find it easier to replace Fe than
 252 those with large radii with the exception of Ti and V.

253 Table 5 shows that only Ti^{4+} , V^{5+} , Cr^{4+} and Mn^{6+} have smaller radii than Nb^{5+} . (The effective
 254 radius of Ni in the 1+ oxidation state is not reported in Shannon's table). Our calculated doping
 255 energies indicate that incorporating V at the Nb site is the easiest process, while the inclusion
 256 of other cations, particularly Cr or Co, is less favourable. However, no discernible relationship
 257 is apparent between the radii of first-row transition metal atoms and their doping energies,
 258 indicating a substantial disparity with the size of Nb, a second-row transition metal atom. In
 259 general, the radii of dopants on the smaller Fe site are larger than on the larger Nb site, except
 260 for Co and Ni, which explains the larger doping energies on the latter site.

261 **Table 5. Shannon effective ionic radii (R) and doping energy (E_d) for the doped FeNbO_4**
 262 **structure.**

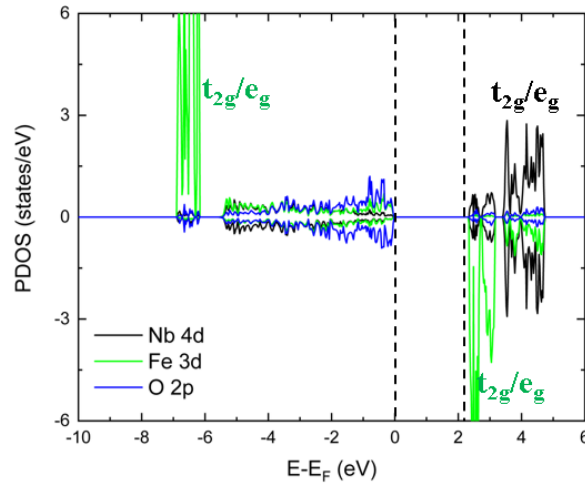
A, B	Fe site		Nb site	
	R (Å)	E_d (eV)	R (Å)	E_d (eV)
Stoichiometric	0.645	-	0.690	-
Ti	0.670	1.67	0.605	2.30
V	0.640	0.85	0.540	1.34
Cr	0.615	0.12	0.550	7.22
Mn	0.645	0.26	0.530	3.60
Co	0.745	1.26	0.745	9.17
Ni	0.690	0.92	-	3.70

263

264 3.1.2 Projected density of states (PDOS)

265 We have plotted the projected density of states (PDOS) for both stoichiometric and doped
 266 FeNbO_4 to elucidate the impact of the first-row transition metal dopants on the electronic
 267 structures. The electronic states of the 1st nearest neighbour (NN) ions to the dopant site were
 268 selected for display, owing to the symmetry of the stoichiometric structure, see Figure S3.
 269 Figure 5 illustrates that stoichiometric FeNbO_4 behaves as a semiconductor with a PDOS band
 270 gap of 2.2 eV. The t_{2g} and e_g valence levels of Fe^{3+} , which are fully occupied, appear at -7 eV
 271 with a separation of ~1.2 eV in the majority spin channel. The empty t_{2g} and e_g states of Fe^{3+}
 272 are located at around 2 eV in the opposite minority spin channel, leading to a separation of 9
 273 eV between them, which is also observed in the previous work on Fe_3O_4 .⁴⁷ Meanwhile, the t_{2g}
 274 and e_g orbitals of Nb are exclusively observed in the conduction band above 3 eV, given that

275 this cation is fully oxidised, having transferred all its 4d electrons to the oxygen anions. The 2p
 276 state of oxygen is delocalised in the valence region, from -5.5 to 0 eV.

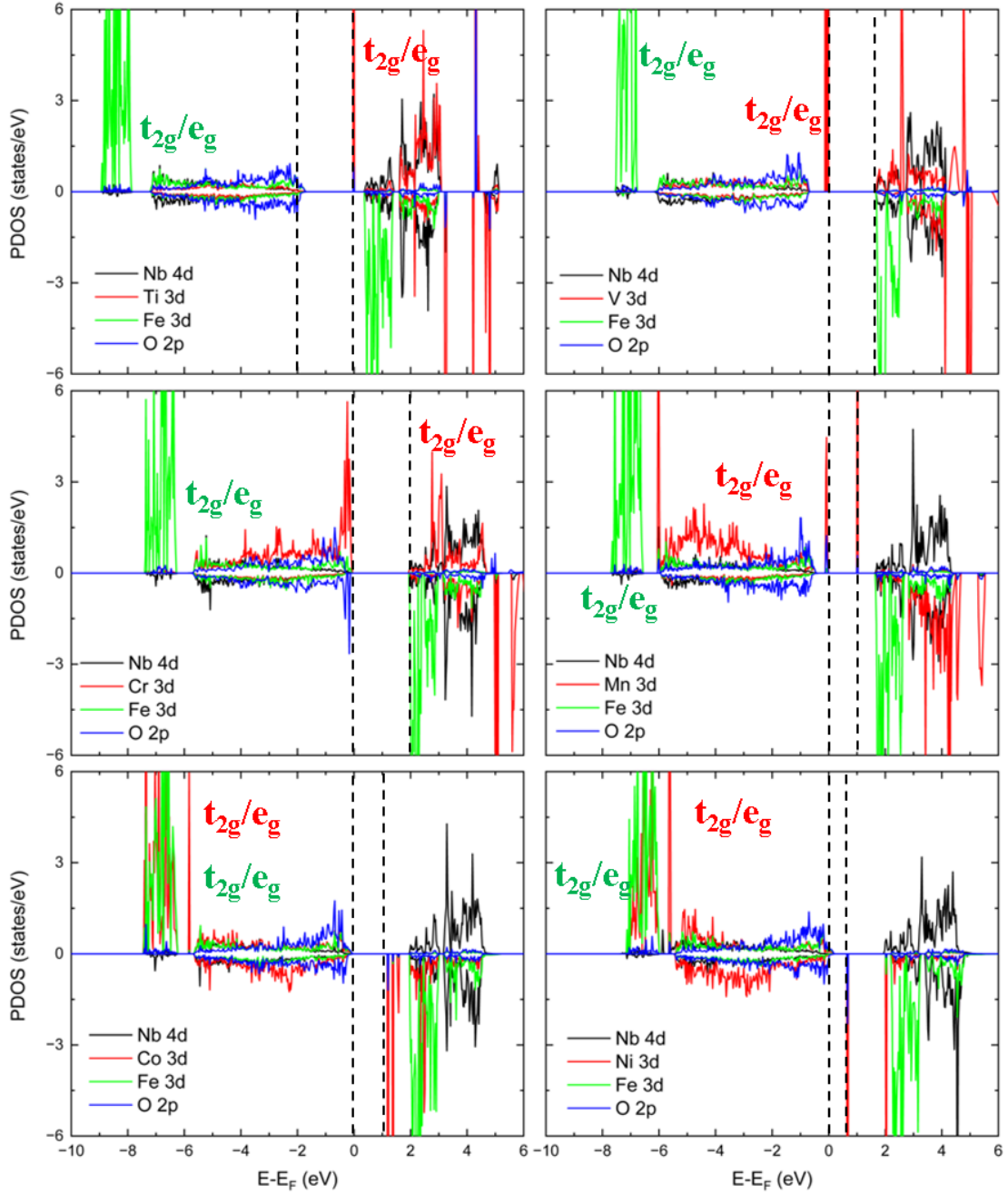


277

278 **Figure 5. Projected density of states (PDOS) for the stoichiometric FeNbO₄.**

279

280 The electronic structure of FeNbO₄ doped at the Fe site with first-row transition metal atoms is
 281 depicted in Figure 6. It is noteworthy that in the Ti-, V- and Cr-doped structures, the t_{2g} valence
 282 orbitals of the dopants progressively shift into the delocalised valence band region. In the Ti-
 283 and V-doped structures, we observe only one localised t_{2g} orbital below the Fermi level, while
 284 in the Cr- to Ni-doped structures, most 3d states are distributed in the valence region from -6
 285 eV to 0 eV. The PDOS of the Co- and Ni-doped structures indicate that the t_{2g} and e_g orbitals
 286 are situated near -7 eV, with the empty e_g orbitals appearing in the conduction band. Our
 287 simulations suggest that with an increase in the atomic number of the dopant, the t_{2g} and e_g
 288 orbitals gradually become fully occupied from Cr to Ni, corresponding to the electronic
 289 occupations of $Ti_{t_{2g}\uparrow}^{eg}$, $V_{t_{2g}\uparrow}^{eg}$, $Cr_{t_{2g}\uparrow\uparrow}^{eg}$, $Mn_{t_{2g}\uparrow\uparrow}^{eg\uparrow}$, $Co_{t_{2g}\uparrow\downarrow\uparrow}^{eg\uparrow\uparrow}$ and $Ni_{t_{2g}\uparrow\downarrow\uparrow\downarrow}^{eg\uparrow\uparrow}$. Additionally, we
 290 found that after doping with Mn, Co or Ni, acceptor levels comprising t_{2g} and e_g orbitals are
 291 generated between the valence band maximum (VBM) and the conduction band minimum
 292 (CBM) of the parent material. Generally, doping proves beneficial in reducing the band gap,
 293 especially for the structure containing Ti on the Fe site, where the Fermi level is close to the
 294 CBM, in agreement with experimental findings²⁸. The impact of dopants on the PDOS of Fe,
 295 Nb and O is negligible with respect to the parent material.



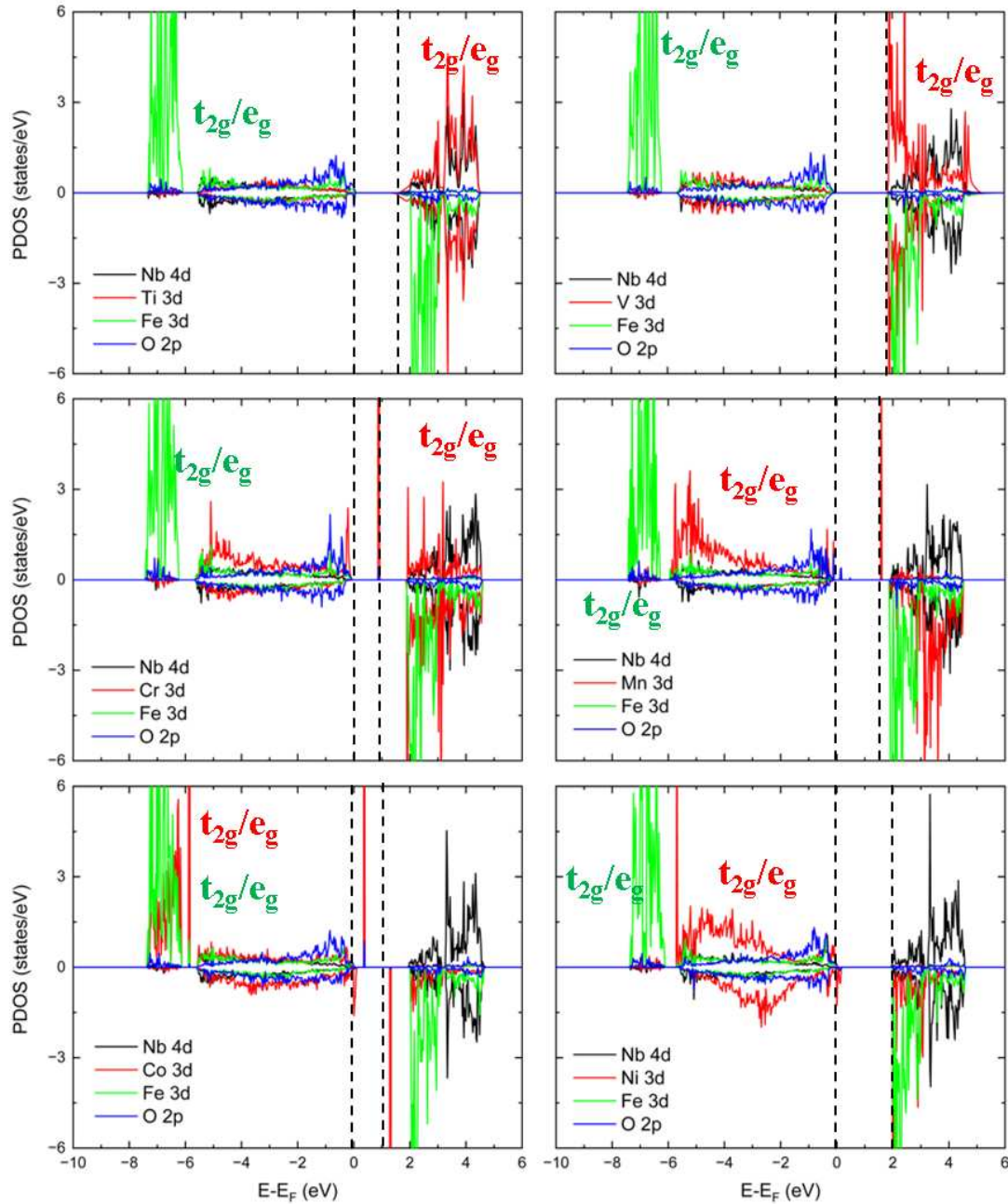
296

297 **Figure 6. Projected density of states (PDOS) of FeNbO₄ doped with (a) Ti, (b) V, (c) Cr, (d) Mn,**
 298 **(e) Co and (f) Ni on the Fe site.**

299

300 Our calculations show that when Ti and V are doped into the Nb site of the stoichiometric
 301 structure, there are no bands in the valence region, as these cations lack electrons. In the Cr-
 302 and Mn-doped structures, the t_{2g} and e_g orbitals appear in the valence band region, but due to
 303 the incomplete occupation of 3d orbitals we still observe states in the conduction band region.

304 With increasing atomic numbers, the electrons in the 3d orbitals of Co- and Ni-doped structures
 305 tend to occupy states further towards -7 eV.-In all the structures, the 3d orbitals of Fe, 4d orbitals
 306 of Nb and 2p orbitals of O show a similar distribution to the parent structure, indicating that the
 307 effect of doping is minimal and can be disregarded.



308

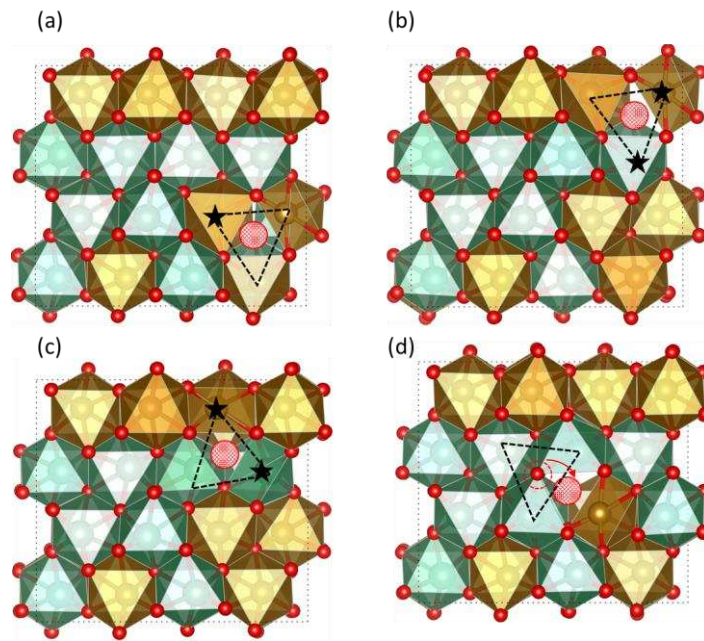
309 **Figure 7. Projected density of states (PDOS) of FeNbO₄ doped with (a) Ti , (b) V , (c) Cr , (d) Mn**
 310 **, (e) Co , and (f) Ni , on the Nb site.**

311 Despite finding that the d-band centres of the dopants appear at particular positions in the DOS,
 312 as well as changes in the cell volume and electronic band gap of the structures owing to the

313 incorporation of transition metal atoms, no trend or relationship between them could be
314 identified, see Tables S2, S3 and S4.

315 **3.2 Effect of dopants on the O-deficient FeNbO₄**

316 Next, we introduced one oxygen vacancy into the supercells and subsequently again
317 incorporated first-row transition metal dopants into the Fe and Nb sites to investigate their effect
318 on the geometric and electronic properties. Figure 8 illustrates four distinct configurations of
319 the O-deficient FeNbO₄ structure, *i.e.* when the oxygen vacancy is surrounded by (i) three Fe
320 (FFF), (ii) two Fe and one Nb (FFN), (iii) one Fe and two Nb (FNN), and (vi) three Nb (NNN)
321 cations. However, we observed that the NNN type oxygen vacancy migrated and transformed
322 into the FNN type following optimization.



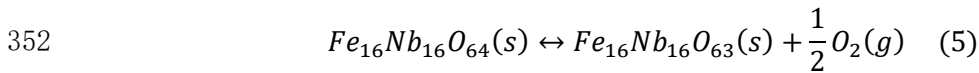
323

324 **Figure 8. Optimised structures of four distinct oxygen vacancy types in the FeNbO₄ structure: (a)**
325 **FFF; (b) FFN; (c) FNN and (d) NNN. The star denotes the selected doping sites; O is red, Fe is**
326 **brown and Nb is green.**

327

328 The lattice parameters of the O-deficient structures are presented in Table 6. Our calculations
329 reveal that the introduction of oxygen vacancies induces an expansion in the lattice parameters
330 *a*, *b*, and *c*. The most significant expansions in *a* and *c* are observed in the FNN-vacancy type
331 structure, while the largest expansion in *b* is found in the FFN-vacancy type structure. Moreover,

332 a slight distortion in the crystal shape is noted, with all angles deviating from 90°, see Table 6.
333 The enlarged lattice parameters and distorted cell shape collectively contribute to a volume
334 expansion in the structure. This expansion can be rationalised by considering the larger size of
335 Fe²⁺ compared to Fe³⁺ cations when the latter undergo reduction upon the formation of an O
336 vacancy, as reported in previous studies^{48,49}. The formation energy of the oxygen vacancy was
337 calculated as: $E_{vac} = E_{Fe_{16}Nb_{16}O_{63}} - E_{Fe_{16}Nb_{16}O_{64}} +$
338 $\frac{1}{2}E_{O_2}$, where $E_{Fe_{16}Nb_{16}O_{63}}$ and $E_{Fe_{16}Nb_{16}O_{64}}$ represent the total energies of the O-deficient
339 FeNbO₄ and stoichiometric FeNbO₄, respectively, and E_{O_2} refers to the total energy of the
340 oxygen molecule in the triplet ground state. The calculated vacancy formation energies indicate
341 that the process is endothermic for the three types of vacancies considered in this study, ranging
342 between 2.14 eV for FFF and 4.13 eV for FNN. This suggests that the material will not
343 spontaneously undergo reduction. The FNN-type vacancy exhibits the largest volume
344 expansion, consistent with its higher number of surrounding Nb atoms. The decreasing order
345 of formation energy for the oxygen vacancies is $E_{vac}^{FNN} > E_{vac}^{FFN} > E_{vac}^{FFF}$. Using the entropy of
346 an O₂ molecule from thermodynamic tables⁵⁰ we have calculated its contribution to the energies
347 at various temperatures. We found that the entropy contribution of half an O₂ molecule is $-T\Delta S$
348 = 2.14 eV at 1580 K, which compensates exactly the energy of -2.14 eV for the process
349 represented in equation (5). Thus, we expect this material to reduce spontaneously between
350 1580 and 1800 K, which is the melting point. Note that we have assumed that the entropy of
351 the bulk solid phases does not change in this analysis



353 **Table 6. Lattice parameters (a, b and c), angles (α, β and γ), volume (V) and formation energy of**
354 **oxygen vacancy (E_{vac}) for the O-deficient FeNbO₄ structure.**

	<i>a</i> (Å)	<i>b</i> (Å)	<i>c</i> (Å)	α (°)	β (°)	γ (°)	V (Å ³)	ΔV/V (%)	E _{vac} (eV)
stoichiometric	9.393	11.367	10.127	90.03	89.93	89.68	1081.339	-	-
FFF	9.409	11.386	10.144	89.94	90.15	89.82	1086.819	0.51	2.14
FFN	9.405	11.383	10.191	90.15	90.27	89.41	1091.086	0.90	3.28
FNN	9.415	11.405	10.180	89.99	89.83	90.17	1093.294	1.10	4.13

355

356 **3.2.1 Structural properties**

357 First, we considered the substitutional doping of one Fe cation surrounding the O vacancy in
358 the FFF-, FFN- or FNN-vacancy type structures, as shown in Figure 9. The calculated magnetic
359 moment, valence state of the first-row transition metal dopant and the doping energy released
360 upon substitution of the structural Fe ion are listed in Table 7. Our simulations indicate that the
361 magnetic moment decreases to $\sim 3.70 \mu_B$ in only two Fe cations in the three types of structures
362 as a result of the formation of the oxygen vacancy. We observe that two 1st NN Fe ions of the
363 oxygen vacancy have a smaller magnetic moment in the FFF and FFN-type structures, whereas
364 one 1st and one 2nd NN cation experience a reduction in the magnetic moment in the FNN-type
365 structure. Although underestimated, the calculated magnetic moment of $\sim 3.7 \mu_B$ corresponds to
366 an electronic distribution of $Fe_{t2g\uparrow\downarrow\uparrow}^{eg\uparrow\uparrow}$ for an octahedral Fe^{2+} , as shown in Figure S4. We found
367 that Ti has the smallest magnetic moment of $\sim 0.80 \mu_B$ of all the dopants considered in this study,
368 where the magnetic moments increase with atomic number of the transition metal from Ti to
369 Mn, which has the largest value of $\sim 4.57 \mu_B$. Our calculations also suggest that the magnetic
370 moment decreases from Mn to Co and from Co to Ni. The electronic distributions of $Ti_{t2g\uparrow}^{eg}$,
371 $V_{t2g\uparrow\uparrow}^{eg}$, $Cr_{t2g\uparrow\uparrow\uparrow}^{eg\uparrow}$, $Mn_{t2g\uparrow\uparrow\uparrow}^{eg\uparrow\uparrow}$, $Co_{t2g\uparrow\downarrow\uparrow\downarrow}^{eg\uparrow\uparrow}$ and $Ni_{t2g\uparrow\downarrow\uparrow\downarrow}^{eg\uparrow\uparrow}$ correspond to the valence states +3,
372 +3, +2, +2, +2 and +2, respectively, see Figure S5-7. Replacing Fe by Mn and Ni dopants is an
373 energetically favourable process compared to introducing Ti, V, Cr and Co dopants, displaying
374 the following decreasing order of doping energies $E_{Ti} > E_V > E_{Cr} > E_{Co} > E_{Mn} > E_{Ni}$.
375 The analysis of the magnetic moments suggests that Fe gains one electron, reducing its valence
376 state from 3+ to 2+, upon the formation of the O vacancy in the stoichiometric material, as
377 shown in Tables 4 and 7. The calculated magnetic moments and valence states of the transition
378 metal dopant atoms are essentially the same in the three types of O-deficient structures.
379 Moreover, we found that the magnetic moments and electronic structures of the dopant atoms
380 are very similar in both $Fe_{0.9375}A_{0.0625}NbO_4$ and $Fe_{0.9375}A_{0.0625}NbO_{3.9375}$, with the exception of
381 the Cr and Mn dopants. The calculated magnetic moment increases from 2.91 to $\sim 3.6 \mu_B$ and
382 from 3.85 to $\sim 4.5 \mu_B$ for Cr and Mn, respectively, suggesting that the formation of the O vacancy
383 reduces these cations from the 3+ to the 2+ oxidation state. Only Cr and Mn display a larger
384 magnetic moment, corresponding to a reduction from 3+ to 2+ with respect to the doped

385 material without O vacancies, in agreement with the charge of the Fe^{2+} that they substituted.
 386 However, Ti and V, which have a valence state of 3+ donated one electron to the 1st or 3rd NN
 387 Fe cations. The doping energy for Ti, V, Cr and Mn (Co and Ni) decreases (increases) from the
 388 FFF to the FFN and from the FFN to the FNN type O-deficient structure. Our calculated doping
 389 energies suggest that replacing Fe with Ti^{3+} and V^{3+} is thermodynamically less favourable than
 390 doping with the other cations in the 3+ oxidation state. We found that the total energy
 391 differences ($E_t = E_{\text{vac}} + E_{\text{doping}}$) between the stoichiometric and doped O-deficient materials are
 392 still larger for the FNN-type structure, with the exception of the Ti-doped phase, indicating that
 393 doping and partial reduction cannot enhance its stability with respect to the FFF and FFN type
 394 structures.

395

396

397 **Table 7. Atomic magnetic moments (m_s), valence states (VS), and doping energy (E_d) and energy**
 398 **differences (E_t) of the O-deficient FeNbO_4 structure with dopants in the Fe site.**

A	FFF (Fe site)				FFN (Fe site)				FNN (Fe site)			
	m_s (μ_B)	VS	E_d (eV)	E_t (eV)	m_s (μ_B)	VS	E_d (eV)	E_t (eV)	m_s (μ_B)	VS	E_d (eV)	E_t (eV)
Fe 1st neigh	3.73 (2)	+2	-	-	3.72(2)	+2	-	-	3.7 (1)	+2	-	-
Fe 3rd neigh	-	-	-	-	-	-	-	-	3.73(1)	+2	-	-
Ti	0.84	+3	3.72	5.86	0.82	+3	3.31	6.59	0.80	+3	2.01	6.14
V	1.89	+3	1.53	3.67	1.86	+3	1.39	4.67	1.84	+3	1.28	5.41
Cr	3.60	+2	0.91	3.05	3.60	+2	0.76	4.04	3.57	+2	0.68	4.81
Mn	4.57	+2	-0.28	1.86	4.56	+2	-0.32	2.96	4.55	+2	-0.34	3.79
Co	2.75	+2	0.27	2.41	2.71	+2	0.35	3.63	2.74	+2	0.36	4.49
Ni	1.74	+2	-0.79	1.35	1.70	+2	-0.68	2.60	1.73	+2	-0.55	3.58

399

400 Next, we introduced dopants on the five-fold Nb sites in proximity to the oxygen vacancies and
 401 subsequently relaxed the structures before computing their properties, as detailed in Table 8.
 402 The FFF-type vacancy structure was not considered for Nb site doping due to the absence of a
 403 1st NN Nb site. Our simulations indicate that magnetic moments remain zero for all Nb atoms
 404 within the FFN and FNN-type vacancy structures. The magnetic moment of the dopants
 405 progressively increases with atomic number from Ti to Mn, while it decreases from Mn to Ni.

406 The magnetic moment configurations for the first-row transition metal atoms correspond to
407 Ti_{t2g}^{eg} , $V_{t2g\uparrow}^{eg}$, $Cr_{t2g\uparrow\uparrow}^{eg}$, $Mn_{t2g\uparrow\uparrow}^{eg\uparrow}$, $Co_{t2g\uparrow\downarrow\uparrow\downarrow}^{eg\uparrow\uparrow}$ and $Ni_{t2g\uparrow\downarrow\uparrow\downarrow}^{eg\uparrow\downarrow}$. We have inferred valence
408 states of +4 for Ti, +4 for V, +3 for Cr, +3 for Mn, +1 for Co and +1 for Ni. Our calculated
409 doping energies reveal that the insertion of Ti, V, and especially Cr and Co into the Nb sites is
410 thermodynamically more difficult than the incorporation of Mn and Ni, with exothermic doping
411 energies of approximately -0.7 and -0.25 eV, respectively. Generally, the generation of oxygen
412 vacancies does not alter the magnetic moment, electronic structure, or oxidation state of Nb^{5+}
413 in $FeNbO_{3.9375}$ compared to $FeNbO_4$. Specifically, the formation of the oxygen vacancy in the
414 doped material leads to changes in the magnetic moments of V, Cr, Mn and Co from 0 to $1 \mu_B$,
415 1.60 to $\sim 2.90 \mu_B$, 3.03 to $\sim 3.80 \mu_B$, and 2.59 to $\sim 2.0 \mu_B$, respectively, corresponding to a
416 reduction of their oxidation states from +5 to +4, +4 to +3, +4 to +3 and +2 to +1, respectively.
417 Furthermore, we observed that the oxidation state of each dopant is smaller than that of the
418 removed Nb^{5+} ion. For instance, the 1+ cations received one electron from each Fe^{2+} and one
419 electron from two 2nd NN O atoms, whereas the 3+ and 1+ cations received charge density from
420 one or two Fe^{2+} ions, respectively. We found that Mn and Ni are the only dopants that can be
421 inserted spontaneously into both the Fe and Nb sites, with Mn displaying a larger preference
422 for the Nb position and Ni for the Fe site. Ti and V are thermodynamically more favourable to
423 dope into the Nb than the Fe site for each vacancy-type structure, whereas Cr and Co
424 preferentially substitute Fe rather than Nb. The largest total energy difference for
425 $FeNb_{0.9375}B_{0.0625}O_{3.9375}$ was calculated for the FNN-type structure, suggesting that doping is
426 unable to modify the order of stability of the doped O-deficient materials.

427

428 **Table 8. Atomic magnetic moments (m_s), valence states (VS), and doping energy (E_d) of the O-**
429 **deficient $FeNbO_4$ structure with dopants incorporated into the Nb site.**

<i>A, B</i>	FFN (Nb site)				FNN (Nb site)			
	m_s (μ_B)	VS	E_d (eV)	E_t (eV)	m_s (μ_B)	VS	E_d (eV)	E_t (eV)
Nb	0	+5	-	-	0	+5	-	-
Ti	0	+4	0.27	3.55	0	+4	0.38	4.51
V	1.00	+4	0.4	3.68	1.00	+4	0.79	4.92
Cr	2.92	+3	5.47	8.75	2.91	+3	4.76	8.89

Mn	3.89	+3	-0.78	2.50	3.84	+3	-0.65	3.48
Co	2.04	+1	5.91	9.19	2.09	+1	5.32	9.45
Ni	1.47	+1	-0.26	3.02	1.45	+1	-0.24	3.89

430

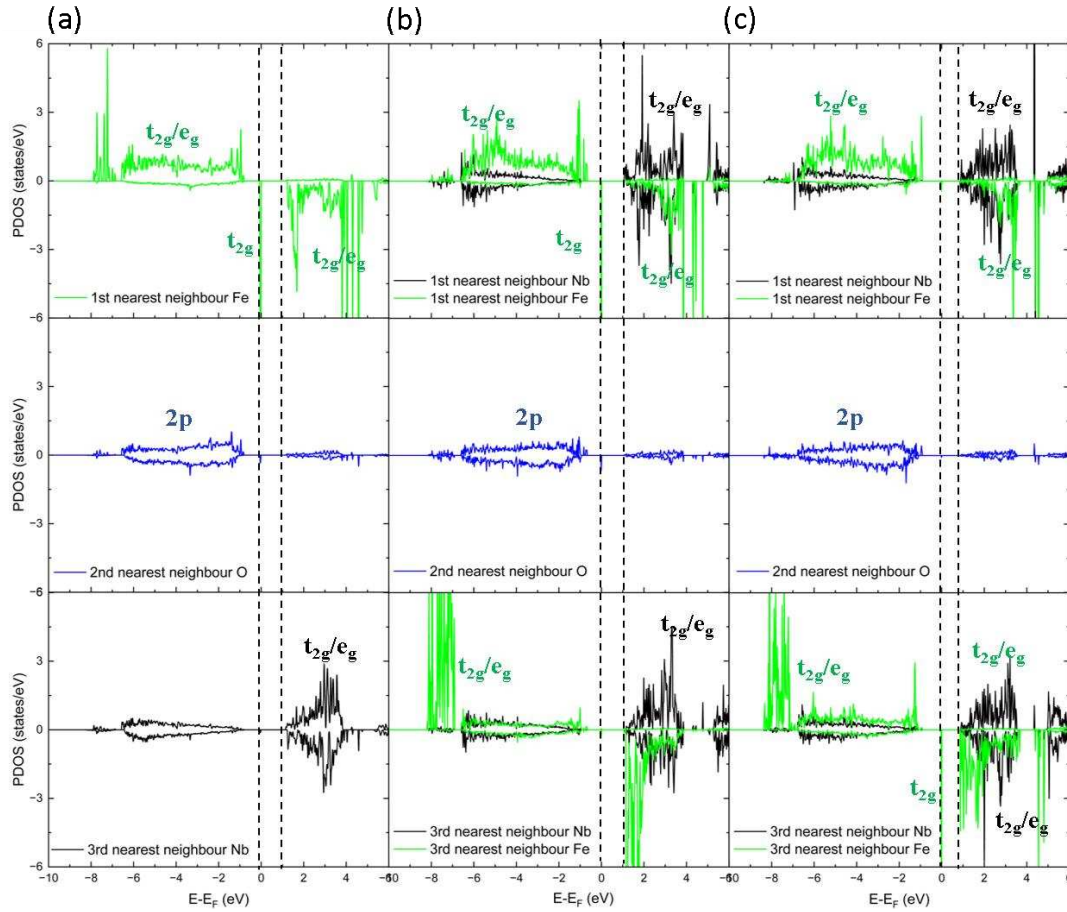
431 **3.2.2 Projected density of states (PDOS)**

432 Here, we discuss the PDOS of ions proximate to the oxygen vacancy in the undoped and doped
 433 structures. In the FFF-vacancy type configuration, we selected the three Fe ions, positioned as
 434 the 1st NN to the O vacancy at approximately 2.0 Å, and the five Nb atoms, situated as the 3rd
 435 NN within the range of 3.2 to 4.0 Å, see Figure S10. In the FFN-vacancy type arrangement, we
 436 focused on the two Fe and the sole Nb cations, serving as the 1st NN of the O vacancy at around
 437 2.0 Å. For the FNN-vacancy type structure, we considered the lone Fe and the two Nb ions,
 438 constituting the 1st NN of the O vacancy at approximately 2 Å. The PDOS was plotted utilising
 439 the twelve O anions from the three vacancy-type structures (2nd NN of the O vacancy between
 440 2.6 and 3.4 Å) as well as the three Fe and two Nb ions from the FFN- and FNN-vacancy type
 441 structures (3rd NN of the O vacancy between 3.4 and 4.4 Å), to plot the PDOS, shown in Figures
 442 S11-13.

443 Figure 9 illustrates that the t_{2g} and e_g levels in the majority spin channel between -8.0 and -1.5
 444 eV are fully occupied for the 1st NN Fe ions of the O vacancy in the FFF-vacancy type structure.
 445 In the FFN-vacancy type structure, the t_{2g} and e_g orbitals of the 1st NN Fe are distributed in the
 446 majority spin region from -7 to -1 eV. Our calculations suggest that the minority spin channel
 447 remains empty in FeNbO₄ for the 1st NN Fe ions in both the FFF- and FFN-vacancy type
 448 structures, with the exception of part of the highly-localised t_{2g} orbital just below the Fermi
 449 level. The t_{2g} and e_g states of the 1st NN Fe are located in the majority spin channel, while the
 450 orbitals in the minority spin channel are unoccupied in the FNN-vacancy type structure. The
 451 majority and minority spin channels of the 3d orbitals of the 1st NN Nb of the O vacancy are
 452 symmetric, and their density of states is smaller for the valence than for the conduction band in
 453 both the FFN- and FNN-type vacancy structures. We found that the full 2p orbitals of all the
 454 2nd NN oxygen remain delocalised from -7 to -1 eV with respect to the stoichiometric material.
 455 For the 3rd NN Nb in the FFF-type vacancy configuration, the negligibly occupied 3d states
 456 appear from -7 to -1 eV, whereas the localised states are above 1.0 eV, similar to the FFN- and

457 FNN-type structures. Our simulations indicate that the t_{2g} and e_g levels of the 3rd NN Fe cations
458 are occupied in the majority spin channel in the FFN- and FNN-type vacancy structures.
459 Interestingly, we found that part of the occupied t_{2g} state of the 3rd NN Fe appears highly-
460 localised below the Fermi level in the FNN-vacancy type structure.

461 Our calculations show that the 1st NN Fe cations of the O vacancy act as donor levels in the
462 FFF- and FFN-type vacancy structures, reducing the bandgap by approximately 1.2 eV
463 compared to the stoichiometric configuration. This behaviour has also been observed in other
464 O-deficient materials such as $\text{LaFe}_{1-x}\text{Nb}_x\text{O}_3$ and $\text{Li}_2\text{FeSiO}_4$ ^{51,52}. However, the electron in this
465 highly-localised orbital is derived from the 3rd NN Fe in the FNN-vacancy type structure,
466 suggesting a preference for electron conduction in the rather more remote area from the FNN-
467 type vacancy. The absence of localised Fe t_{2g} and e_g states around -8 eV implies the absence of
468 Fe^{3+} in the vicinity of the vacancy sites, specifically in the 1st NN region of the FFN- and FNN-
469 type structures. Our calculations indicate that the 3d electronic states of Nb, regardless of their
470 positions, slightly hybridize with the 2p orbitals of oxygen in the valence band, similar to the
471 stoichiometric FeNbO_4 . Consequently, we opted not to discuss their density of states in the
472 subsequent sections.



473

474 **Figure 9. Projected density of states (PDOS) for FeNbO₄ with different types of oxygen vacancies**
 475 **(a) FFF; (b) FFN and (c) FNN.**

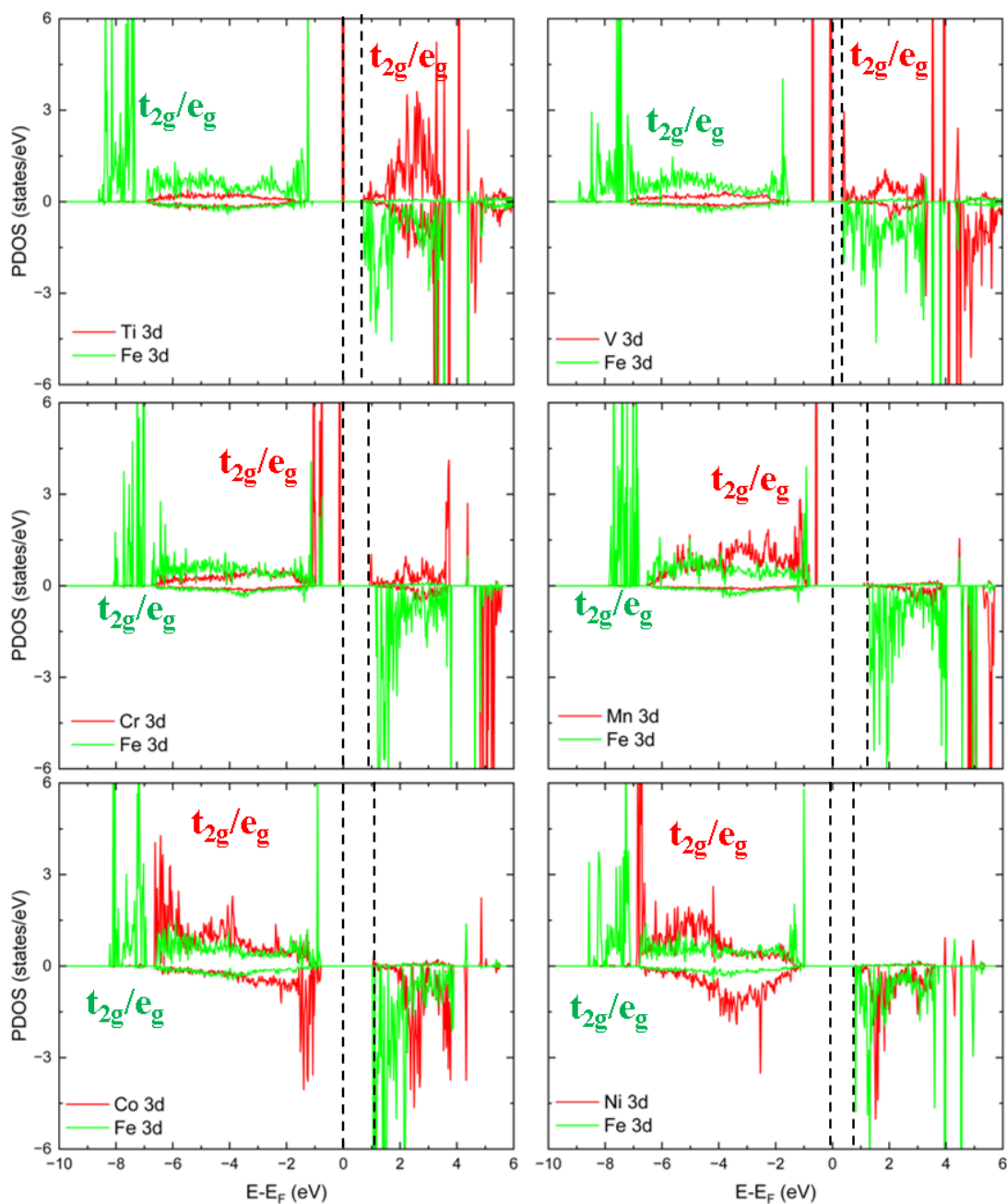
476

477 First, we have simulated the PDOS for Fe_{0.9375}A_{0.0625}NbO_{3.9375} structures, containing FFF-, FFN-,
 478 and FNN-type vacancies, respectively, see Figure S13-15. Overall, we found that the electronic
 479 states of the dopants and Fe cations exhibited similar distributions in the three types of oxygen-
 480 vacancy structures. In this context, we chose to analyse only the PDOS of the doped FFF-
 481 vacancy type configuration to investigate the effect of dopants on the electronic structures.

482 Figure 10 illustrates that the 3d orbitals of the 1st NN Fe occupy the majority spin channel from
 483 -8 to -1 eV, while the minority spin channel remains unfilled above 1 eV in all the doped
 484 structures. Electronic states of Ti, V, and Co dopants are primarily distributed in the conduction
 485 region, with one, two and four sharp orbitals, respectively, appearing below the Fermi level.
 486 The majority spin channel of the Mn dopant is fully occupied, while its minority spin channel
 487 is in the conduction region. The t_{2g} and e_g levels of the Co and Ni dopants are present in both

488 the majority and minority spin channels in the valence region, and part of the conduction band
489 remains unoccupied over 1 eV. In general, our simulations reveal that the highly-localised states
490 of Fe^{2+} below 0 eV are replaced by the t_{2g} orbitals of the Ti, V, and Cr dopants, reducing the
491 band gap to less than 0.5 eV, especially for the Ti- and V-doped structures. In contrast, the t_{2g}
492 and e_g levels of the Mn, Co, and Ni dopants shift towards the deep region of the valence band,
493 resulting in no states around the Fermi levels, consistent with observations in doped TiO_2 as
494 well³⁸⁻⁴⁰. Overall, comparing with the doped $\text{Fe}_{0.9375}\text{A}_{0.0625}\text{NbO}_4$ structures, we observe that the
495 electronic states of Ti and V remain similarly allocated in both doped configurations. On the
496 other hand, the highly-localised orbitals of Cr and Mn are generated below the Fermi levels in
497 the O-deficient structures. The electronic states of the Co and Ni dopants tend to be delocalised
498 in the valence region from -7 to -1 eV in the $\text{Fe}_{0.9375}\text{A}_{0.0625}\text{NbO}_{3.9375}$ structures, rather than being
499 concentrated around -8 eV in the $\text{Fe}_{0.9375}\text{A}_{0.0625}\text{NbO}_4$ configurations.

500



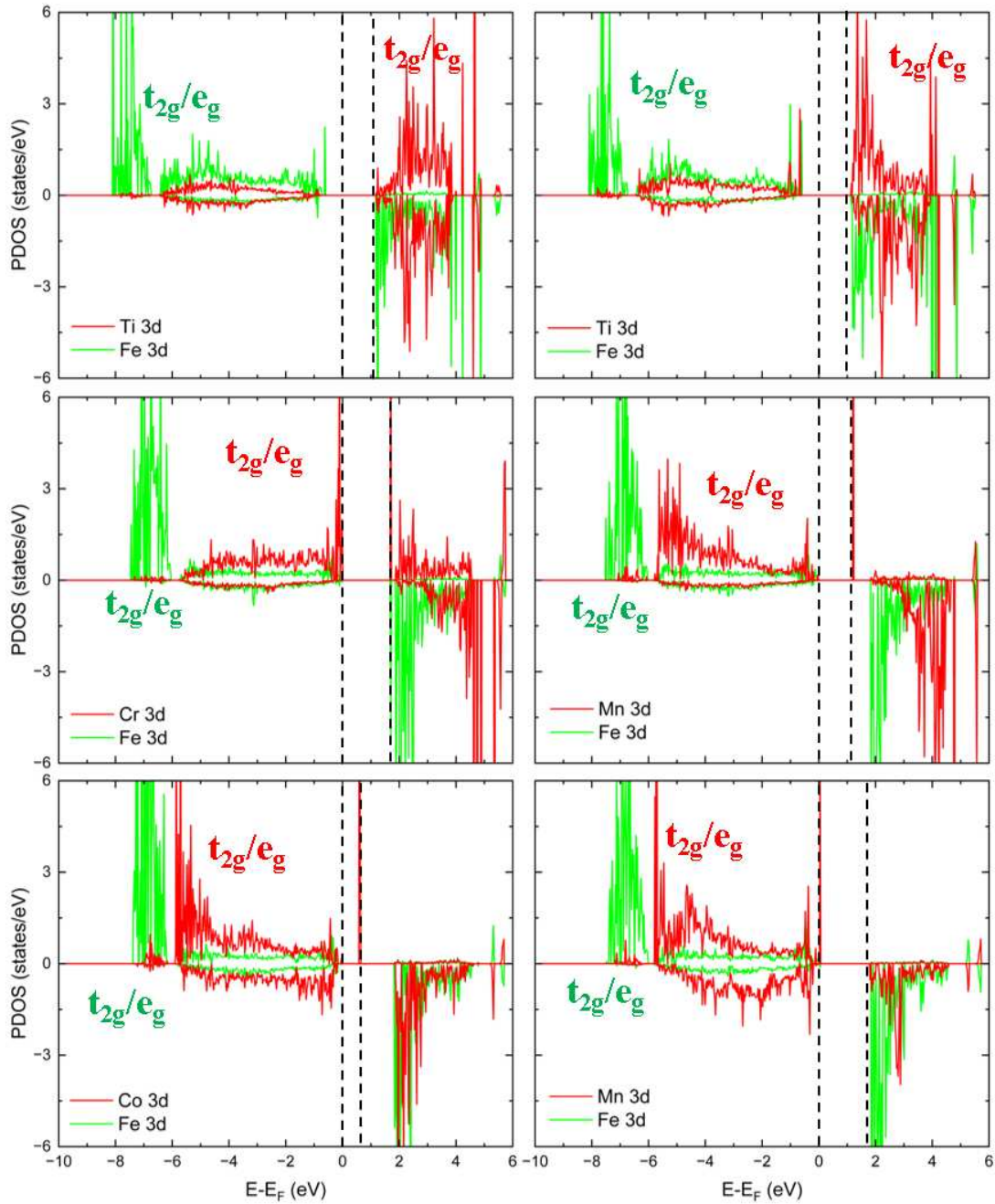
501

502 **Figure 10. Projected density of states (PDOS) for dopants and the 1st nearest neighbour (NN) Fe**
 503 **in the FFF-type $\text{Fe}_{0.9375}\text{A}_{0.0625}\text{NbO}_{3.9375}$ structures featuring (a) Ti, (b) V, (c) Cr, (d) Mn, (e) Co,**
 504 **and (f) Ni dopants on the Fe site.**

505

506 We also selected the PDOS of the FFN-type $\text{FeNb}_{0.9375}\text{B}_{0.0625}\text{O}_{3.9375}$ materials to illustrate their
 507 electronic structures, see Figure 11, as they exhibit similar distributions to the FNN-type, see
 508 Figure S16 and 17. We observe that the occupied states of the Fe cations are distributed from -

509 8 to -1 eV for the Ti- and V-doped structures, and from -8 to 0 eV for the Cr-, Mn-, Co- and
510 Ni-doped structures. The t_{2g} and e_g levels of the Ti and V dopants predominantly occupy both
511 the majority and minority spin channels in the conduction region, except for the localised t_{2g}
512 orbitals of V near the VBM. Specifically, a sharp level is observed in the CBM of the Cr-doped
513 structure, and this type of highly-localised orbitals shifts towards the Fermi levels with an
514 increase in atomic numbers from Cr to Ni. In general, our calculations demonstrate the removal
515 of highly-localised orbitals of the Fe cations below the Fermi levels in the Ti- and V-doped
516 structures. Moreover, we found no evidence of Fe^{2+} in the Cr-, Mn-, Co- and Ni-containing
517 structures, indicating that it has been oxidized back to Fe^{3+} after doping. Furthermore, acceptor
518 levels are generated and tend to move close to the Fermi levels in the Cr- to the Ni-doped
519 structures. During this process, we observe a reduction in the bandgap to 0.5 eV for the Co-
520 doped structure, while it remains relatively large at -1.8 eV for the Cr- and Ni-doped structures,
521 even exceeding that of the undoped O-deficient structures. When comparing with the
522 $FeNb_{0.9375}B_{0.0625}O_4$ structure, we found that the electronic states distributions of Ti dopants
523 remain the same, whereas the additional localised levels of V dopants are situated in the VBM
524 after the generation of oxygen vacancies. The acceptor level, composed of the 3d orbitals of Cr
525 tends to move towards the CBM after the creation of oxygen vacancies. For the Mn-, Co-, and
526 Ni-doped configurations, the impact of the oxygen vacancy on the electronic structures of the
527 dopant is negligible and can be disregarded.



528

529 **Figure 11. Projected density of states (PDOS) of the dopants, the 1st and 3rd nearest neighbour**
 530 **(NN) Fe in the FFN-type $\text{Fe}_{0.9375}\text{A}_{0.0625}\text{NbO}_{3.9375}$ structures with (a) Ti, (b) V, (c) Cr, (d) Mn, (e)**
 531 **Co, and (f) Ni dopants on the Nb site.**

532

533 4. Conclusions

534 We have conducted DFT calculations of the $\text{Fe}_{0.9375}\text{A}_{0.0625}\text{NbO}_4$ and $\text{FeNb}_{0.9375}\text{B}_{0.0625}\text{O}_4$
 535 materials, where A, B = Ti, V, Cr, Mn, Co and Ni, as well as the O-deficient

536 $\text{Fe}_{0.9375}\text{A}_{0.0625}\text{NbO}_{3.9375}$ and $\text{FeNb}_{0.9375}\text{B}_{0.0625}\text{O}_{3.9375}$ structures (A, B = Ti, V, Cr, Mn, Co and Ni).
537 Our calculations indicate that substituting the Fe cation with these dopants is considerably more
538 energetically favourable than the Nb site, leading to significant compression of
539 $\text{FeNb}_{0.9375}\text{B}_{0.0625}\text{O}_4$, except for the Ti-doped configuration. Doping Ti, V, and Mn at the Fe site
540 of the stoichiometric structure transforms it into an n-type semiconductor, while the Co- and
541 Ni-doped $\text{FeNb}_{0.9375}\text{B}_{0.0625}\text{O}_4$ structures shift to p-type semiconductors.

542 In the O-deficient structure, random distribution of cations occurs, resulting in the identification
543 of three stable types of oxygen vacancies, *i.e.* FFF-, FFN-, and FNN-type vacancies. Our
544 calculations have shown that the stability of O-deficient configurations depends on the number
545 of 1st NN Nb atoms at the O vacancy. For instance, generating the FFF-type vacancy is less
546 endothermic than the FNN-type vacancy, leading to the largest volume expansion. Overall, for
547 the doping process in the Fe or Nb sites surrounding the vacancies, we observe that the type of
548 oxygen vacancies does not significantly affect the structural properties and electronic structures
549 of the dopants. However, the presence of an oxygen vacancy can alter the oxidation state and
550 doping energies relative to the $\text{Fe}_{0.9375}\text{A}_{0.0625}\text{NbO}_4/\text{FeNb}_{0.9375}\text{B}_{0.0625}\text{O}_4$ structures. For instance,
551 the order of doping energies in the Fe sites of the non-vacancy configurations is as follows:
552 $E_{\text{Ti}^{3+}} > E_{\text{Co}^{2+}} > E_{\text{Ni}^{2+i}} > E_{\text{V}^{3+}} > E_{\text{Mn}^{3+}} > E_{\text{Cr}^{3+}}$, whereas in the O-deficient structures, the
553 sequence becomes: $E_{\text{Ti}^{3+}} > E_{\text{V}^{3+}} > E_{\text{Cr}^{2+}} > E_{\text{Co}^{2+}} > E_{\text{Mn}^{2+}} > E_{\text{Ni}^{2+}}$. Furthermore, it is
554 noteworthy that doping Ti and V into the Fe sites of the O-deficient structures could
555 significantly enhance electronic conduction by moving the donor levels close to the CBM.
556 However, doping these first-row transition metals into the Nb site surrounding the vacancies
557 tends to shift the structures towards p-type semiconductors, especially for the Co-doped
558 configurations, where the bandgap narrows from 1.0 to 0.5 eV.

559

560 **5. Supplementary Material**

561 The Supplementary Materials include the structural information of metal oxides used for
562 calculating doping energies, the relationship between volume change, band-gap and d-band

563 centre, the magnetic configurations, the octahedral field of splitting, the selected sites for
564 doping atoms, and the PDOS plots of the O-deficient structures.

565

566 **6. Acknowledgements**

567 Xingyu Wang acknowledges the China Scholarship Council (CSC) [No. 201906460008] and
568 the University of Leeds for the award of a PhD scholarship. This work has used the computing
569 resources from the Supercomputing Wales project, which is partly funded by the European
570 Regional Development Fund (ERDF), and the high-performance computing facilities (ARC4)
571 provided by the University of Leeds. We also acknowledge computing resources on the UK's
572 national supercomputing service ARCHER2 facility (<http://www.archer2.ac.uk>) via our
573 membership of the UK's HEC Materials Chemistry Consortium, which is funded by EPSRC
574 (EP/L000202).

575 **Data availability**

576 The data that support the findings of this study are available within the article and the
577 supplementary material.

578

References

579

- 580 1. Ananta, S., Brydson, R., Thomas, N. W., Synthesis, "Formation and Characterisation of
581 FeNbO₄ Powders," J. Eur. Ceram. Soc. 19, 489-496 (1999).
- 582 2. Theissmann, R., Ehrenberg, H., Weitzel, H., Fuess, H., Domain Structure and Lattice
583 Strains in FeNbO₄. Solid State Sci 7, 791-795 (2005).
- 584 3. Theissmann, R., Ehrenberg, H., Weitzel, H., Fuess, H., "Nanostructured Cation
585 Distribution in FeNbO₄:A Synchrotron Powder Diffraction and Transmission Electron
586 Microscopy Investigation," J. Mater. Sci. 37, 4431-4436 (2002).
- 587 4. Saritha, D., "Sol-Gel Synthesis and Electrochemical Properties of Wolframite FeNbO₄,"
588 J. Phys.: Conf. Ser. 1495, 012019 (2020).
- 589 5. Balamurugan, C., Maheswari, A. R., Lee, D. W., Subramania, A., "Selective Ethanol Gas
590 Sensing Behavior of Mesoporous N-Type Semiconducting FeNbO₄ Nanopowder Obtained by
591 Niobium–Citrate Process," Current Applied Physics 14, 439-446 (2014).
- 592 6. Kanti Biswas, S., Gnanasekaran, T., Kumar Ghorai, T., Pramanika, P., "Sensing Properties
593 of Chemically Synthesized Pristine and Pt-Impregnated Nanosized FeNbO₄ in Hydrogen,
594 Ammonia, and Lpg," J. Electrochem. Soc. 155, J26-J31 (2008).
- 595 7. Gnanasekar, K. I., Jayaraman, V., Prabhu, E., Gnanasekaran, T., Periaswami, G.,
596 "Electrical and Sensor Properties of FeNbO₄ : A New Sensor Material," Sens. Actuators, B 55,
597 170-174 (1999).
- 598 8. A Harrison, W. T., Cheetham, A. K., "Structural and Magnetic Properties of FeNbO₄-II,"
599 Chemical Crystallography Laboratory, University of Oxford, 24, 523-527 (1988).
- 600 9. Alvarez, G., Font, R., Portelles, J., Raymond, O., Zamorano, R., "Paramagnetic Resonance
601 and Non-Resonant Microwave Absorption in Iron Niobate," Solid State Sci. 11, 881-884
602 (2009).
- 603 10. Raymond, O., Font, R., Suárez-Almodovar, N., Portelles, J., Siqueiros, J. M., "Frequency-
604 Temperature Response of Ferroelectromagnetic Pb(Fe_{1/2}Nb_{1/2})O₃ Ceramics Obtained by
605 Different Precursors. Part I. Structural and Thermo-Electrical Characterization," *Journal of*
606 *Applied Physics* 97, 084108 (2005).

- 607 11. Li, Q. J., "The Colossal Dielectric Properties of FeNbO₄," *Journal of Alloys and*
608 *Compounds* 616, 577-580 (2014).
- 609 12. Devesa, S., Graça, M. P., Henry, F., Costa, L. C., "Dielectric Properties of FeNbO₄
610 Ceramics Prepared by the Sol-Gel Method," *Solid State Sci.* 61, 44-50 (2016).
- 611 13. Devesa, S., Graça, M. P., Costa, L. C., "Microwave Dielectric Properties of the Binary
612 System BiNbO₄- FeNbO₄," *ECS J. Solid State Sci. Technol.* 9 093010 (2020).
- 613 14. Sri Devi Kumari, T., Vinith Gandhi, R., Rahul, G., Kamalanathan, G., Prem Kumar, T.,
614 Jeyakumar, D., Lakshminarasimhan, N., "Electrochemical Lithium Insertion Behavior of
615 FeNbO₄: Structural Relations and in Situ Conversion into FeNb₂O₆ During Carbon Coating,"
616 *Mater. Chem. Phys* 145, 425-433 (2014).
- 617 15. Wang, T., Shi, S., Kong, F., Yang, G., Qian, B., Yin, F., -The Role of Stable Interface in
618 Nano-Sized FeNbO₄ as Anode Electrode for Lithium-Ion Batteries," *Electrochim. Acta* 203,
619 206-212 (2016).
- 620 16. Wang, T., Ge, T., Shi, S., Wu, M., Yang, G., "Synthesis of Wolframite FeNbO₄ Nanorods
621 as a Novel Anode Material for Improved Lithium Storage Capability," *J. Alloys Compd.*
622 740, 7-15 (2018).
- 623 17. Ni, C., Feng, J., Cui, J., Zhou, J., Ni, J., "An n-Type Oxide Fe_{0.5}Mg_{0.25}Ti_{0.25}Nb_{0.9}Mo_{0.1}O₄
624 Δ for Both Cathode and Anode of a Solid Oxide Fuel Cell," *J. Electrochem. Soc.* 164, F283-
625 F288 (2017).
- 626 18. Zhang, H., Kim, Y. K., Jeong, H. Y., Lee, J. S., "A Few Atomic FeNbO₄ Overlayers on
627 Hematite Nanorods: Microwave-Induced High Temperature Phase for Efficient
628 Photoelectrochemical Water Splitting," *ACS Catal.* 9, 1289-1297 (2018).
- 629 19. Liu, X., Xie, D., Irvine, J. T. S., Ni, J.; Ni, C., "An FeNbO₄-Based Oxide Anode for a Solid
630 Oxide Fuel Cell (SOFC)," *Electrochim. Acta* 335, 135692 (2020).
- 631 20. Liu, X., Zhou, J., Xie, D., Ni, J., Ni, C., "FeNbO₄-Based Oxide Cathode for Steam
632 Electrolysis," *Solid State Ionics* 345, 115181 (2020).
- 633 21. Ahmed, S. H., Bakiro, M., Alzamly, A., "Visible-Light-Driven Photocatalytic Formation
634 of Propylene Carbonate Using FeNbO₄/Reduced Graphene Oxide Composites," *Materialia* 12,
635 100781 (2020).

- 636 22. Leiva, H., Sieber, K., Khazai, B., Dwight, K., Wold, A., "Structural and Electronic
637 Relationships between Conducting Iron Niobates and Iron Tungstates," J. Solid State Chem.
638 25, 113-118 (1982).
- 639 23. Schmidbauer, E., "Electrical Resistivity, Thermopower, and Fe Mossbauer Study of
640 FeNbO₄," J. Solid State Chem. 134, 253-264 (1997).
- 641 24. He, S., Dai, H., Cai, G., Chen, H., Guo, L., "Optimization of La_{0.75}Sr_{0.25}Cr_{0.5}Mn_{0.5}O_{3-Δ}-
642 Ce_{0.8}Sm_{0.2}O_{1.9} Compositionally Graded Anode Functional Layer," Electrochim. Acta 152, 155-
643 160 (2015).
- 644 25. Ye, X.-F., Wang, S. R., Wang, Z. R., Hu, Q., Sun, X. F., Wen, T. L., Wen, Z. Y., "Use of
645 La_{0.75}Sr_{0.25}Cr_{0.5}Mn_{0.5}O₃ Materials in Composite Anodes for Direct Ethanol Solid Oxide Fuel
646 Cells," J. Power Sources 183, 512-517 (2008).
- 647 26. Zhang, S., Wan, Y., Xu, Z., Xue, S., Zhang, L., Zhang, B., Xia, C., "Bismuth Doped
648 La_{0.75}Sr_{0.25}Cr_{0.5}Mn_{0.5}O_{3-Δ} Perovskite as a Novel Redox-Stable Efficient Anode for Solid Oxide
649 Fuel Cells," J. Mater. Chem. A 8, 11553-11563 (2020).
- 650 27. Gan, L., Ye, L., Ruan, C., Chen, S., Xie, K., "Redox-Reversible Iron Orthovanadate
651 Cathode for Solid Oxide Steam Electrolyzer," Adv. Sci. 3, 1500186 (2016).
- 652 28. Kousi, K., Tang, C., Metcalfe, I. S., Neagu, D., "Emergence and Future of Exsolved
653 Materials," Small 17, e2006479 (2021).
- 654 29. Cowin, P. I., Lan, R., Zhang, L., Petit, C. T. G., Kraft, A., Tao, S., "Study on Conductivity
655 and Redox Stability of Iron Orthovanadate," Mater. Chem. Phys. 126, 614-618 (2011).
- 656 30. Wang, X., De Leeuw, N. H., Santos-Carballal, D., "Oxygen Diffusion in the Orthorhombic
657 FeNbO₄ Material: A Computational Study," Phys. Chem. Chem. Phys. 25, 6797-6807 (2023).
- 658 31. Wang, X., Santos-Carballal, D., de Leeuw, N. H., "Density Functional Theory Study of
659 Monoclinic FeNbO₄: Bulk Properties and Water Dissociation at the (010), (011), (110), and
660 (111) Surfaces," J. Phys. Chem. C 125, 27566-27577 (2021).
- 661 32. Ahmed, S. H., Bakiro, M., Alzamy, A., "Effect of Ph and Surfactant on Band Gap
662 Properties of Monoclinic FeNbO₄ Prepared Via Different Routes," Nano-Struct. Nano-Objects
663 20, 100400 (2019).

- 664 33. John, K., Bijan, K., Jacob, H., Robert, K., Kirby, D., Aaron, W., "Preparation and
665 Photoelectronic Properties of FeNbO₄," J. Solid State Chem. 35, 128-132 (1980).
- 666 34. Kresse, G., Furthmüller, J., "Efficiency of Ab-Initio Total Energy Calculations for Metals
667 and Semiconductors Using a Plane-Wave Basis Set," Comput. Mater. Sci. 6, 15-20 (1996).
- 668 35. Kresse, G., Furthmüller, J., "Efficient Iterative Schemes for Ab Initio Total-Energy
669 Calculations Using a Plane-Wave Basis Set," Phys. Rev. B Condens. Matter 54, 11169-11186
670 (1994).
- 671 36. Kresse, G., Hafner, J., "Ab Initio Molecular Dynamics for Open-Shell Transition Metals,"
672 Phys. Rev. B Condens. Matter 48, 13115-13118 (1993).
- 673 37. Kresse, G., Hafner, J., "Norm-Conserving and Ultrasoft Pseudopotentials for First-Row
674 and Transition Elements," J. Phys.: Condens. Matter 6, 8245-8260 (1994).
- 675 38. Blochl, P. E., "Projector Augmented-Wave Method," Phys. Rev. B Condens. Matter 50,
676 17953-17979 (1994).
- 677 39. Vega, A., Dorantes-Davila, J., Balbas, L. C., Pastor, G. M., "Calculated Sp-Electron and
678 Spd-Hybridization Effects on the Magnetic Properties of Small Fe_n Clusters," Phys. Rev. B
679 Condens. Matter 47, 4742-4746 (1993).
- 680 40. Diéguez, O., Alemany, M. M. G., Rey, C., Ordejón, P., Gallego, L. J., "Density-Functional
681 Calculations of the Structures, Binding Energies, and Magnetic Moments of Fe Clusters with 2
682 to 17 Atoms," Phys. Rev. B 63, 205407 (2001).
- 683 41. Perdew, J. P., Burke, K., Ernzerhof, M., "Generalized Gradient Approximation Made
684 Simple," Phys. Rev. Lett. 77, 3865-3868 (1996).
- 685 42. Dudarev, S. L., Botton, G. A., Savrasov, S. Y., Humphreys, C. J., Sutton, A. P., "Electron-
686 Energy-Loss Spectra and the Structural Stability of Nickel Oxide: An LSDA+U Study," Phys.
687 Rev. B 57, 1505-1509 (1998).
- 688 43. Henkelman, G., Arnaldsson, A., Jónsson, H., "A Fast and Robust Algorithm for Bader
689 Decomposition of Charge Density," Comput. Mater. Sci. 36, 354-360 (2006).

- 690 44. Luong, H. D., Momida, H., Dinh, V. A., Oguchi, T., "Understanding Doping Effects on P₂
691 Na_xMn_{1-y}M_yO₂(M=Li, Mg, Al, Ti, V, Cr, Fe, Co, Ni) Cathode Materials for Na-Ion Batteries,"
692 Phys. Rev. Mater. 6, 015802 (2022).
- 693 45. Prasad, R., Benedek, R., Thackeray, M. M., "Dopant-Induced Stabilization of
694 Rhombohedral LiMnO₂ against Jahn-Teller Distortion," Phys. Rev. B 71, 134111 (2005).
- 695 46. Halcrow, M. A., "Jahn-Teller Distortions in Transition Metal Compounds, and Their
696 Importance in Functional Molecular and Inorganic Materials," Chem. Soc. Rev. 42, 1784-1795
697 (2013).
- 698 47. Santos-Carballal, D., Roldan, A., Grau-Crespo, R., de Leeuw, N. H., "A DFT Study of the
699 Structures, Stabilities and Redox Behaviour of the Major Surfaces of Magnetite Fe₃O₄," Phys.
700 Chem. Chem. Phys. 16, 21082-97 (2014).
- 701 48. Aidhy, D. S., Liu, B., Zhang, Y., Weber, W. J., "Chemical Expansion Affected Oxygen
702 Vacancy Stability in Different Oxide Structures from First Principles Calculations," Comput.
703 Mater. Sci. 99, 298-305 (2015).
- 704 49. Choudhury, B., Choudhury, A., "Ce³⁺ and Oxygen Vacancy Mediated Tuning of Structural
705 and Optical Properties of CeO₂ Nanoparticles," Mater. Chem. Phys. 131, 666-671 (2012).
- 706 50. M. W. J. Chase, "NIST JANAF Thermochemical Tables, American Chemical Society and
707 American Institute of Physics for the National Institute of Standards and Technology,"
708 Washington DC, 1998.
- 709 51. Zhou, Y., Lü, Z., Li, J., Xu, S., Xu, D., Wei, B., "The Electronic Properties and Structural
710 Stability of LaFeO₃ Oxide by Niobium Doping: A Density Functional Theory Study," Int. J.
711 Hydrogen Energy 46, 9193-9198 (2021).
- 712 52. Zhang, L., Wu, S., Shuai, J., Hou, Z., Zhu, Z., "Formation of Oxygen Vacancies in
713 Li₂FeSiO₄: First-Principles Calculations," Phys. Chem. Chem. Phys. 23, 20444-20452 (2021).